

Tracking of single charge carriers in a conjugated polymer nanoparticle

*Jiangbo Yu, Changfeng Wu[†], Zhiyuan Tian[‡], Jason McNeill**

Department of Chemistry, Clemson University, SC 29634, USA

Email address: mcneill@clemson.edu

EXPERIMENTAL AND METHODS

Preparation and Characterization of Nanoparticle.

The polyfluorene derivative PFBT (MW 10,000, polydispersity 1.7) was purchased from ADS Dyes, Inc. (Quebec, Canada). Tetrahydrofuran (THF, HPLC grade, 99.9%) and glycerol (99.5%) were purchased from Sigma-Aldrich (Milwaukee, WI). All chemicals were used without further purification. For preparation of PFBT dots, 10 mg of the conjugated polymer PFBT was dissolved in 10 g of HPLC grade tetrahydrofuran (THF) by stirring overnight under inert atmosphere. The solution was then filtered through a 0.7 micron glass fiber filter in order to remove any insoluble material. Then 200 μ L of the solution was injected by pipette into 8 mL water under mild sonication. The THF was removed by partial vacuum evaporation, and aggregates were removed by filtration through a 220 nm PTFE membrane filter. Typically, less than 10% of the polymer was removed by filtration of the suspension, as determined by UV-Vis absorption spectroscopy, indicating that most of the polymer formed nanoparticles. For the determination of particle size by AFM, one drop of the nanoparticle dispersion was placed on a freshly cleaved mica substrate. After evaporation of the water, the surface topography was imaged with an Ambios Q250 AFM in AC mode, yielding an average number of 15.0 ± 4.4 nm for the PFBT nanoparticle diameter (shown in Figure S1).

* Corresponding author, Email address: mcneill@clemson.edu.

[†]: Currently in Department of Chemistry, University of Washington, Seattle, WA 98195

[‡]: Currently in College of Chemistry and Chemical Engineering, Graduate University of the Chinese Academy of Sciences (GUCAS), Beijing, P. R. China 100049.

Single Particle Imaging and Tracking.

Single particle imaging and tracking were performed on a customized wide-field epifluorescence microscope described as follows. The 473 nm laser beam from a diode pumped CW blue laser (Laser Lab Components, BL473-50) is guided onto the epillumination port of an inverted fluorescence microscope (Olympus IX-71). Inside the microscope, the laser beam is reflected by a 500 nm long-pass dichroic mirror (Chroma 500 DCLP), and focused onto the rear aperture of a high numerical aperture objective (Olympus Pl Ach, 100 \times , 1.25 NA, Oil). The laser excitation at the sample focal plane exhibits a nearly Gaussian profile with a FWHM of $\sim 5 \mu\text{m}$. Typical employed laser intensities were approximately 70 W/cm^2 in the center of the laser spot in the sample plane, as estimated based on the measured laser power, size of the excitation spot, and transmission of the objective. Nanoparticle fluorescence is collected by the objective lens, reflected by a 500 nm long-pass dichroic mirror (Chroma 500 DCLP), filtered by two 500 nm longpass filters (Andover), and then refocused by an achromat lens onto a back-illuminated frame transfer EMCCD camera (Princeton Instruments, PhotonMAX: 512B), yielding a pixel resolution of 105 nm/pixel. A closed loop *xyz* piezoelectric scanning stage (P-517.3CL, Polytec PI) was used to position particles within the laser spot and for fine adjustment of focus. An image acquisition rate of 50 Hz was employed. An overall microscope fluorescence detection efficiency of $\sim 3\%$ was determined using Nile red loaded polystyrene spheres (Invitrogen) as standards. For the single particle tracking, PFBT conjugated nanoparticles (CPNs) were fixed on a coverslip and kept under N_2 protection during the entire tracking process. Determination of lateral (*x,y*) position, width, and integrated intensity of the fluorescence spots was performed using custom scripts written for Matlab (Mathworks, Natick, MA), where fitting to a 2D Gaussian was performed using a least-squares algorithm. The centroid positions of the single CPNs obtained from the fit were corrected for position fluctuations due to vibration and air flow as follows. Typically 8-15 particles were visible in a given image, and only the particles with brightness within roughly 1σ of the average were flagged for tracking analysis. Typically, the 2-3 brightest particles exhibited steady fluorescence (minimal blinking), and the fluctuations in their centroid positions were highly correlated with one another, consistent with vibration of the sample. Thus the brighter particles in the image were

used for vibration-correction, after additional statistical tests to ensure that the fluctuations in their position centroids were not affected by particle dynamics. The correction for the vibration of each frame was calculated by averaging the centroid positions of the 2-3 brightest particles in the frame. The correction was subtracted from the centroid positions of the particles of interest in each frame.

Determination of tracking uncertainty

The initial estimate of the tracking uncertainty based on per-particle fluorescence intensity levels was obtained as follows. Assuming the tracking uncertainty is due to a combination of photon counting noise and the focal characteristics of the imaging setup, the tracking uncertainty δ is given by the expression ¹

$$\delta = \sqrt{\frac{\sigma^2}{N} + \frac{a^2/12}{N} + \frac{8\pi\sigma^4b^2}{a^2N^2}},$$

where σ is the width of the point spread function, a is the size of the pixel, b is the background noise, and N is the number of detected photons per image. For example, a typical nanoparticle emits detected photons of $N = 176,000$, and the microscope configuration gives $\sigma = 273$ nm, $a = 105$, and the background noise is roughly $b = 18$, yielding a tracking uncertainty for this nanoparticle of $\delta = 0.7$ nm, according to the above equation. This result is in agreement with the measurement uncertainty obtained from the root mean square displacement analysis of typically <1 nm at minimum lag time.

Determination of fluorescence cross-section

The fluorescence cross-section of a CPN σ_f is calculated by the formula $\sigma_f = k_p / I_{ex} / \eta_c$, where k_p is the CCD detected photon rate, I_{ex} is the laser excitation power density, η_c is the whole microscope collection efficiency, and $k_p = I_i / t / \eta_{CCD}$, where I_i is the initial brightness (photons) of the nanoparticle, t is the exposure time for the image, and η_{CCD} is the CCD quantum efficiency.

Determination of quenching efficiency of single hole polaron (Q_p)

The quenching efficiency for a hole polaron is determined from the corrected intensity trajectory. In order to correct the intensity trajectory for photobleaching dynamics, the intensity trajectory was first fit to a biexponential ($y = A_1e^{-x/\tau_1} + A_2e^{-x/\tau_2} + y_0$) and then the intensity was divided by the fitted biexponential results. The resulted intensity values

were further normalized by their mean number. This yielded a curve with a mean of 1 with intensity fluctuations given as a fraction of the running average intensity (Figure S3). Finally, the quenching efficiency was assumed to be equal to the standard deviation (STD) of the corrected intensity.

SUPPLEMENTARY RESULTS AND DISCUSSION

AFM and photoluminescence characterization results of the CPNs

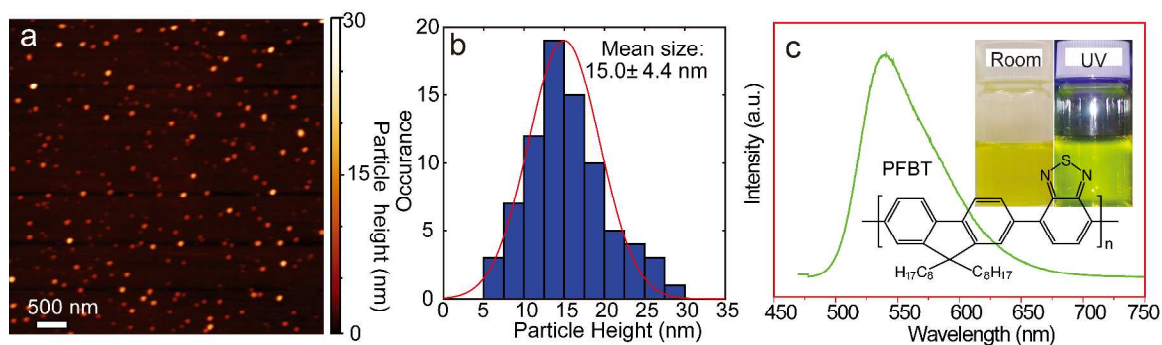


Figure S1. (a) AFM image of PFBT nanoparticles. (b) Histogram of nanoparticle size distribution. (c) The photoluminescence spectra of PFBT nanoparticles in water solution at an excitation wavelength of 456 nm. One insert is the chemical structure of the PFBT polymer, the other is a photograph of PFBT nanoparticles with the mean size of 15 nm suspended in water under room light and UV light.

The fluorescence intensity trajectories for single CPNs with different fluorescence cross-sections

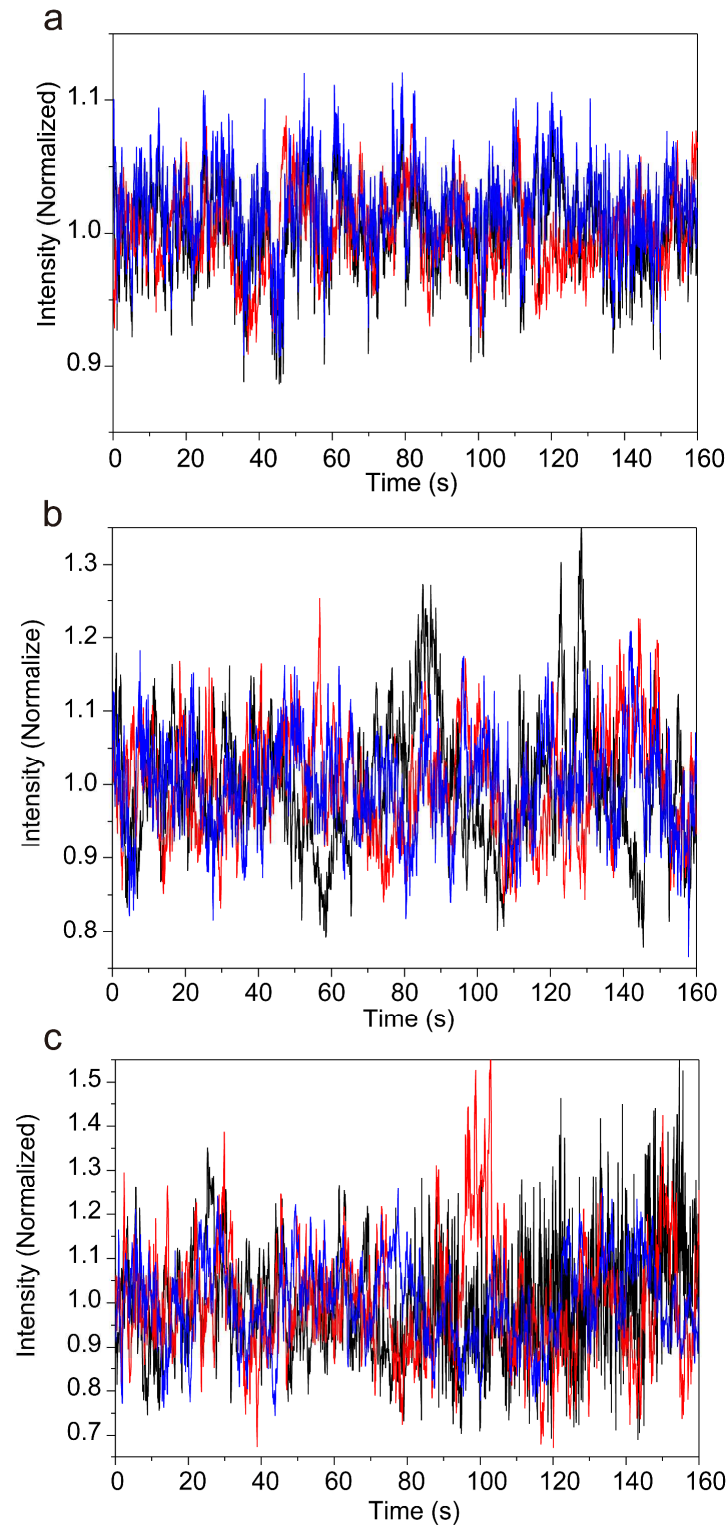


Figure S2. Several normalized intensity trajectories showing major “types”: (a) high fluorescence cross-section (bright); (b) medium fluorescence cross-section; (c) low fluorescence cross-section (dim).

From these trajectory plots, a relationship between the fluorescence intensity fluctuations and the brightness of single CPNs is evident: CPNs with lower brightness (i.e., smaller CPNs) show higher fluctuation amplitude. For CPNs with brightness classified as low, medium and high, the standard deviations of the fluorescence intensities are around 13%, 8% and 3%, respectively. These results are qualitatively consistent with quenching by hole-polarons, since the exciton diffusion model predicts that the quenching efficiency per polaron decreases as the nanoparticle size increases.

Effect of photobleaching on the mean square displacement

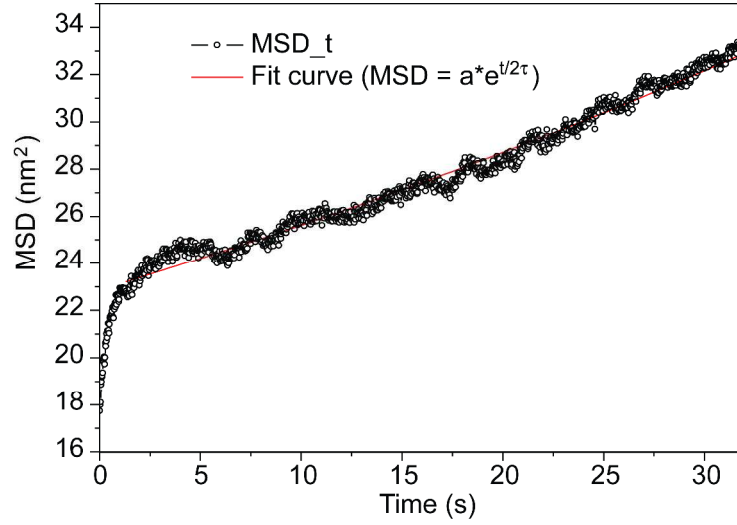


Figure S3. The plot $MSD(t)$ of the long period time, and its fitting line (red solid) at the period from 2.0 to 32 s by the function $MSD = ae^{t/2\tau}$ (the fitted result is $a = 9.3$ and $\tau = 38.5$ s)

Fig. S3 shows the mean square displacement, $MSD(t)$, out to roughly 30 s. At long lag times (after roughly 2 s), MSD increases slowly due to irreversible photobleaching. Irreversible photobleaching decreases the number of photons per particle per frame (N), which increases the uncertainty of position (Δx , and $\Delta x \propto 1/\sqrt{N}$). N decreases exponentially over time due to the photobleaching. Therefore, at long times, the MSD increases exponentially as $MSD = ae^{t/2\tau}$, where τ is the photobleaching time constant. After fitting the $MSD(t)$ curve between 2 and 32 s to the above functional form, the fitted results are obtained as $a = 9.3 \text{ nm}^2$ and $\tau = 38.5$ s.

The intensity autocorrelation at early versus late time

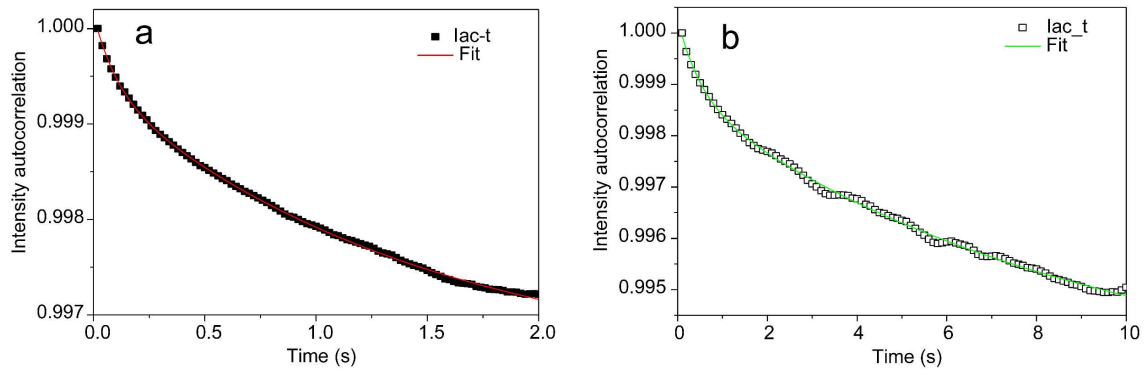


Figure S4. The fluorescence intensity autocorrelation curves and their fits to the bi-exponential formula ($y = A_1 e^{-x/\tau_1} + A_2 e^{-x/\tau_2} + y_0$): a), for 2s period time the fitting yields red solid line and $\tau_1 = 0.10$ s, $\tau_2 = 1.46$ s, $A_1 = 0.001$, $A_2 = 0.003$; b), for 10s period time the fitting yields a green solid line and $\tau_1 = 0.51$ s, $\tau_2 = 8.73$ s, $A_1 = 0.001$, $A_2 = 0.006$.

The results of the fits to the stretched-exponential and power law functions of fluorescence intensity and centroid autocorrelation curves

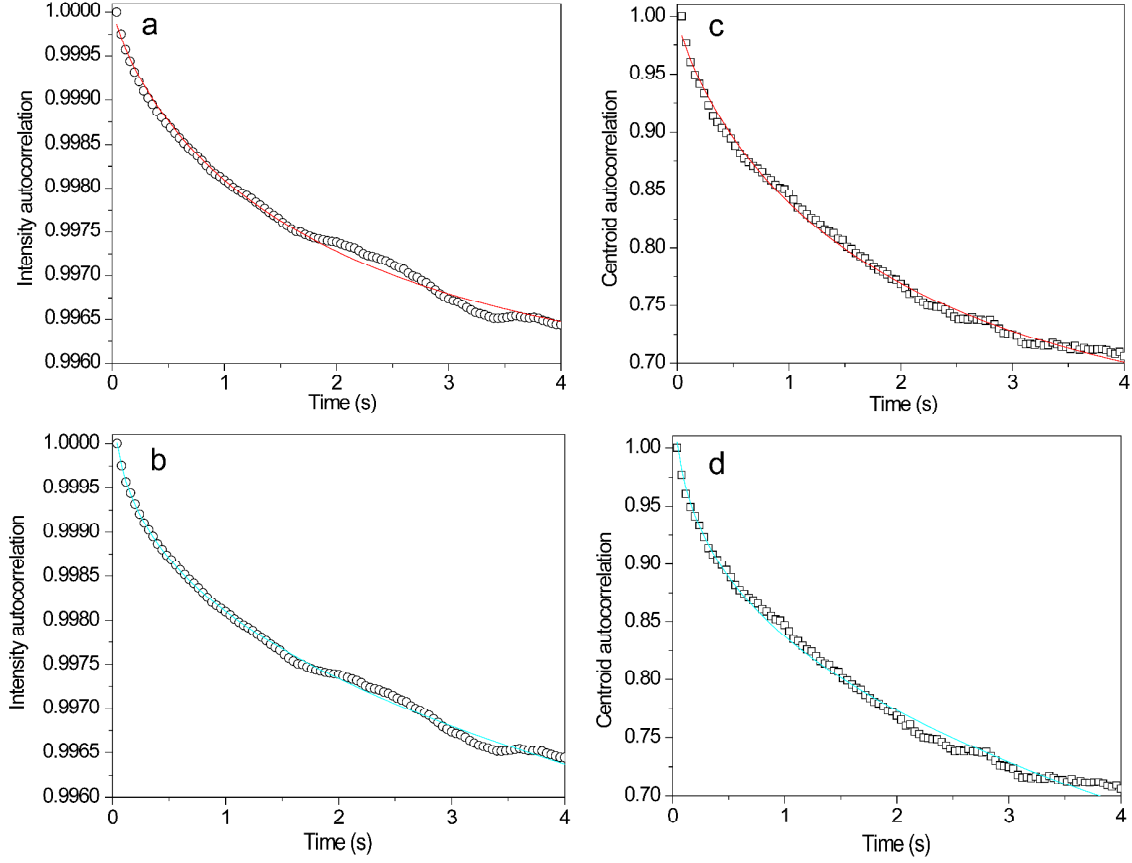


Figure S5. The fluorescence intensity (a and b) and centroid autocorrelation curves (c and d) and their fits to the stretched-exponential function (red lines, $I(t) = I(0) + Ae^{-(t/\tau)^\beta}$): for a), $A = 0.0043$, $\tau = 1.98$ s, $\beta = 0.75$; for c), $A = 0.36$, $\tau = 1.96$ s, $\beta = 0.79$. They were also fitted by power law model (cyan lines, $I(t) = I(0) + At^b$): for b), $A = -0.0029$, $b = 0.34$; for d), $A = -0.26$, $b = 0.32$.

Intensity and position autocorrelations - dependence on particle size

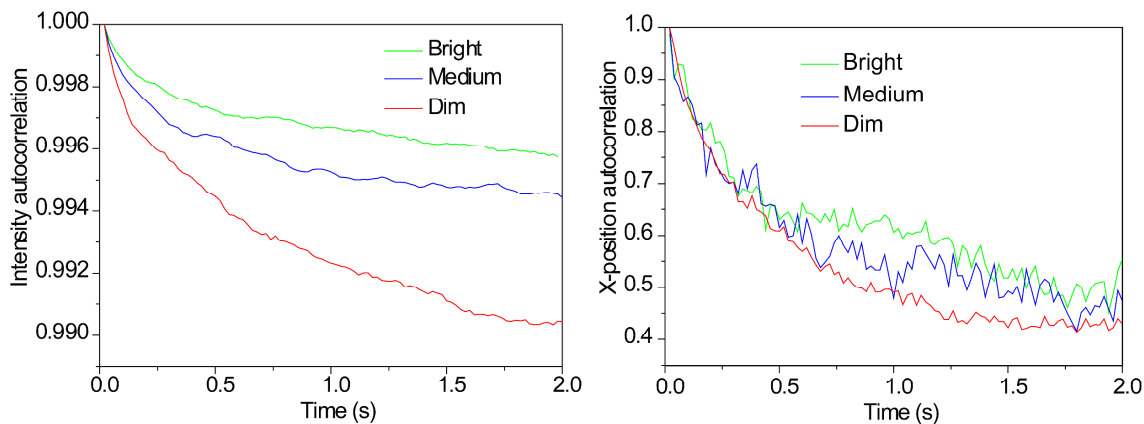


Figure S6. Stack plot of normalized intensity and position autocorrelations of the fluorescence centroid of nanoparticles with different FL cross-section (i.e., bright (green), medium (blue) and dim (red) at moderate laser intensity: (a) intensity autocorrelation; (b) x -position autocorrelation.

Figure S6 displays normalized autocorrelations of the fluorescence intensity and centroid position of three different single CPNs with different brightness (bright, medium and dim, corresponding to large, medium, and small CPNs, respectively). The dimmer (smaller) nanoparticles clearly show higher fluctuation amplitude of the intensity autocorrelation curve, and the position fluctuations show a similar, but less pronounced size effect. The higher amplitude of the fluctuation in relative intensity of the smaller particles is consistent with a higher quenching efficiency for polarons in smaller particles, and is also evident from visual inspection of the intensity trajectories.

The corrected and normalized fluorescence intensity trajectory of single nanoparticle

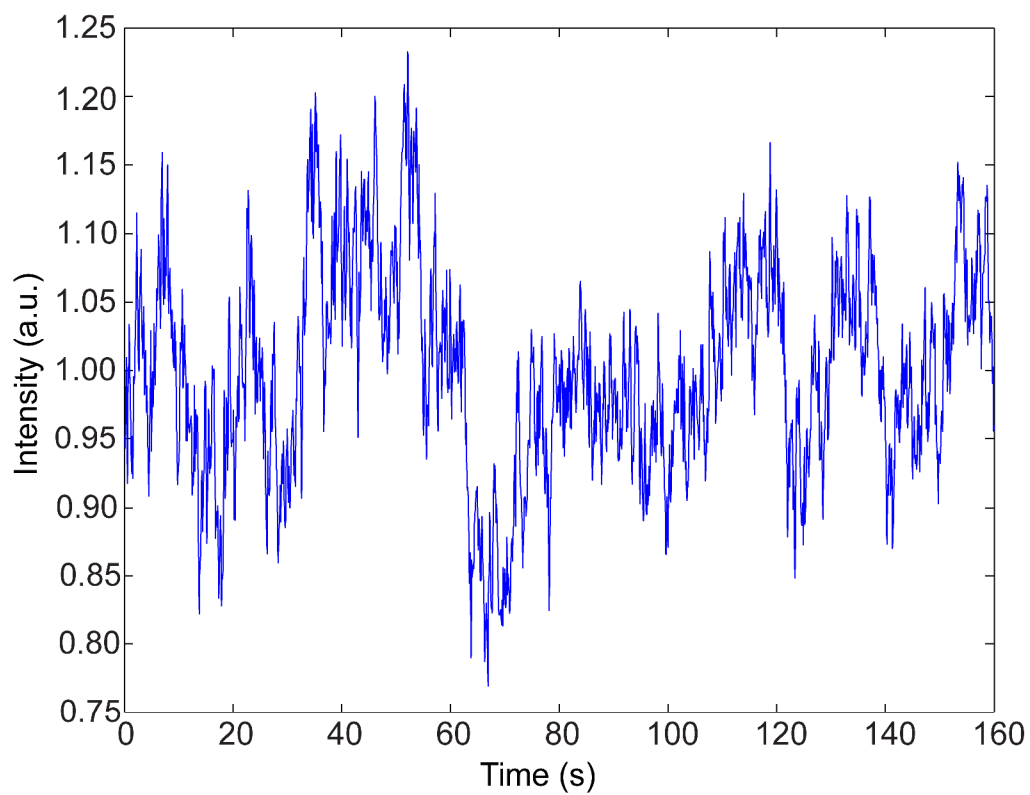


Figure S7. The corrected and normalized fluorescence intensity trajectory of the single CPN shown in Figure 2.

Effect of multiple polarons on the measured diffusion constant

The expressions in the article relating fluctuations in the fluorescence centroid of the nanoparticle were obtained assuming a single polaron. However, it is likely that in some cases there are several polarons present in the CPN, each contributing to fluctuations in the fluorescence centroid of the nanoparticle. Here we consider an approximate model to estimate the effect of multiple polarons on the mean square displacement. We represent the system consisting of nanoparticle and polarons as a 1D finite lattice with N occupied sites, representing the fluorescent particle, and p vacancies, representing the polaron and surrounding quenched polymer, which are assumed to be mobile. The fluorescence centroid of the system is represented by the center of mass of the system. The presence of a single polaron at position x will result in a displacement of the centroid by x/N . The presence of several polarons would result in a shift in the center of mass of

$$\frac{1}{N} \sum_{i=1}^p x_i \quad . \quad (1)$$

where the factor $1/N$ corresponds to the quenching efficiency of the polaron. A collection of polarons/vacancies, each undergoing a random walk, yields a mean square displacement of the center of mass of

$$\langle X^2(\tau) \rangle = \sum_{i=1}^p \langle x_i^2(\tau) \rangle = p \langle x_1^2(\tau) \rangle \quad . \quad (2)$$

Thus the presence of additional polarons will tend to increase the measured mean square displacement, by a factor equal to the number of polarons.

Effect of polaron generation and recombination on fluorescence centroid

It is plausible that the fluctuations in the fluorescence centroid at early lag times are due to fluctuations in the number of polarons, since photogeneration of polarons and polaron recombination are known to occur in conjugated polymers, and changes in the polaron population are thought to be responsible for the reversible photoquenching observed in CPNs.^{2,3} Additionally, the time constants associated with the intensity autocorrelation at early times are similar to those of the centroid autocorrelation. However, this similarity could be due to other effects, such as differences in quenching efficiency as a polaron moves from one site to another. Indeed, the quenching model predicts that the quenching efficiency of polarons decreases slowly with radial distance, within a few nm of the surface (Figure 4). Assuming polarons are more or less evenly distributed throughout the particle and most hopping events are short range (<2 nm), then most hopping events either have a small radial component or occur well away from the surface, thus the fluctuations in intensity due to polaron motion are expected to be relatively small. This is consistent with the experimental observation that the autocorrelation of the experimental intensity is typically >99% flat, as shown in Figure 3. As an additional test of the hypothesis that the fluctuations in centroid are due to changes in the number of polarons, we performed cross-correlation calculations and visually inspected the trajectories. If a significant fraction of the fluctuations in centroid were due to fluctuations in polaron number, then one would expect to observe either significant cross-correlation, or a significant fraction of centroid jumps coincident with intensity jumps. However, no significant cross-correlation between intensity and position $\langle \delta I \delta x \rangle$ or $\langle (\delta I \delta x)^2 \rangle$ was observed, and visual comparison of the trajectories indicates that jumps in position typically (though not always) occurred without a simultaneous change in intensity. Finally, we consider whether the timescales of the fluctuations are consistent with other measures of polaron generation and recombination dynamics. Based on previous results,³ the lifetime of polarons in CPNs is roughly 20-30 s in inert atmosphere at room temperature. Based on the fact that the excitation intensity is well below saturation, we estimate that there are typically fewer than 10 polarons per nanoparticle. Thus, at steady-state, the estimated number of polaron generation or recombination events per nanoparticle per second is in the range of 0.03 to 1 (a time between generation or

recombination events of 1-30 s). This is more an order of magnitude slower than the timescale for polaron diffusion observed in the mean-square displacement (roughly 0.2 s, Figure 2).

Model and simulations of effect of hole polaron on nanoparticle fluorescence centroid

In order to estimate the effect of a hole polaron at a given position, acting as a fluorescence quencher, on the fluorescence centroid of a nanoparticle, we performed simulations of exciton diffusion and energy transfer on a 3D lattice. The parameters employed in the simulations were the exciton diffusion length (set to 5 nm), the Forster radius of the quencher (set to 2 nm), the size of the nanoparticle (set to 16 nm dia.), the quencher position, and the lattice spacing. This set of parameters yielded good agreement with experimental quenching efficiencies. Two different approaches to calculate the effect of the quencher on the fluorescence centroid were employed. Initially, an approach based on a random walk representation of exciton diffusion and energy transfer was employed, as discussed in previous publications.⁴ However, our implementation of this calculation method is quite slow (several days of computer time were required for a single calculation), and so a more computationally efficient approach was pursued, based on the steady-state approximation. The calculations were set up and performed as follows. The diffusion equation was expressed as coupled rate equations for each point on a 3D grid. Terms for the rate of energy transfer to the quencher for each point on the grid were added, based on the distance from each grid point to the quencher. The steady-state approximation was employed, resulting in a set of coupled linear equations. The coupled linear equations were expressed as a sparse matrix and solved using an iterative conjugate gradient squared method, using MATLAB. Calculations were completed within a few seconds for a $64 \times 64 \times 64$ grid. Increasing the grid density to yield $128 \times 128 \times 128$ grid points yielded results similar to those obtained using a $64 \times 64 \times 64$ grid, indicating that the grid density was adequate. The steady-state results were also similar to those obtained using the random walk approach, indicating that the steady-state approximation is valid for this system. Calculations were performed for polaron positions ranging from 0 to 8 nm relative to the center of the grid, and the quenching efficiencies and displacements of the fluorescence centroid were calculated, yielding the results shown in Figure 4.

REFERENCES

1. Thompson, R. E.; Larson, D. R.; Webb, W. W., Precise nanometer localization analysis for individual fluorescent probes. *Biophys. J.* 2002, 82 (5), 2775-2783.
2. Yu, J.; Song, N. W.; McNeill, J. D.; Barbara, P. F., Efficient Exciton Quenching by Hole Polarons in the Conjugated Polymer MEH-PPV. *Isr. J. Chem.* 2004, 44, 127.
3. Tian, Z. Y.; Yu, J. B.; Wu, C. F.; Szymanski, C.; McNeill, J., Amplified energy transfer in conjugated polymer nanoparticle tags and sensors. *Nanoscale* 2010, 2 (10), 1999-2011.
4. Wu, C. F.; Zheng, Y. L.; Szymanski, C.; McNeill, J., Energy transfer in a nanoscale multichromophoric system: Fluorescent dye-doped conjugated polymer nanoparticles. *Journal of Physical Chemistry C* 2008, 112 (6), 1772-1781.

Table S1. Some physical parameters for some selected typical nanoparticles.

Particle	D_f^a ($\times 10^{-14}$ cm ² /s)	L_f^b (nm)	I_i^c ($\times 10^5$ photons)	σ_f^d ($\times 10^{-12}$ cm ²)	Q_p^e (%)	D_p^f ($\times 10^{-11}$ cm ² /s)	μ_p^g ($\times 10^{-10}$ cm ² /V·s)
1	12.09	2.20	1.85	4.0	8.4	1.71	6.7
2	6.87	2.17	1.02	1.8	6.6	1.58	6.2
3	20.60	3.35	1.73	2.4	8.4	2.92	11.4
4	11.5	2.91	1.58	2.6	9.7	1.22	4.8
5	4.95	2.01	1.05	1.9	11.0	0.41	1.6
6	9.78	2.45	1.76	2.7	10.2	0.94	3.7
7	2.77	1.32	1.48	2.1	9.0	0.34	1.3
8	4.95	1.84	1.24	1.7	7.6	0.86	3.4
9	5.39	1.99	1.76	3.2	7.3	1.01	3.9

Note:

^a Diffusion coefficient of the fluorescence centroid obtained from a fit to the equation $\langle x_f^2(\tau) \rangle = \langle x_f^2(0) \rangle + L_f^2 \{1 - \exp(-2D_f\tau/L_f^2)\}$ for the mean-square-displacement (x_f) of a particle undergoing confined diffusion.

^b Confinement length of the fluorescence centroid obtained from a fit to the equation $\langle x_f^2(\tau) \rangle = \langle x_f^2(0) \rangle + L_f^2 \{1 - \exp(-2D_f\tau/L_f^2)\}$ for the mean-square-displacement (x_f) of a particle undergoing confined diffusion.

^c The initial brightness of the single nanoparticle expressed by the detected photons in the first frame.

^d The fluorescence cross-section of a CPN σ_f is calculated by the formula: $\sigma_f = k_p / I_{ex} / \eta_c$, where k_p is the rate of photon detection, I_{ex} is the laser excitation power density, η_c is the overall microscope collection efficiency, and $k_p = I_i / t / \eta_{CCD}$, where I_i is the initial brightness (photons) of the nanoparticle, t is the exposure time for the image, η_{CCD} is the CCD quantum efficiency.

^e The quenching efficiency estimated from the standard deviation of the corrected intensity of the exciton fluorescence centroid.

^f The diffusion coefficient of the quenching hole polaron, which is calculated from the diffusion coefficient of the fluorescence centroid and the estimated quenching efficiency (Q_p) according to the intensity autocorrelation: $D_p = D_c / Q_p^2$.

^g The hole-polaron mobility calculated based on the Stokes-Einstein equation ($D = \mu k_B T$) and the D_p .